

## Article

# The Calcite-Dolomite Solvus Temperature and T-X(CO<sub>2</sub>) Evolution in High-Grade Impure Marble from Thongmön Area, Central Himalaya: Implications for Carbon Cycling in Orogenic Belts

Xueqian Chen, Lifei Zhang \*, Guibin Zhang and Zeng Lü

MOE Key Laboratory of Orogenic Belts and Crustal Evolution, School of Earth and Space Sciences, Peking University, Beijing 100871, China; chenxueqian@pku.edu.cn (X.C.); gbzhang@pku.edu.cn (G.Z.); luzeng@pku.edu.cn (Z.L.)

\* Correspondence: lfzhang@pku.edu.cn

**Abstract:** Impure dolomitic marble from the Great Himalayan Sequences (GHS) in Thongmön area, central Himalaya, is first systematically reported here concerning its petrographic features, textural relations, and fluid evolution. The Thongmön impure marble is characterized by the assemblage of calcite + dolomite + forsterite + spinel + phlogopite + clinohumite ± diopside ± retrograde serpentine. Three groups of calcite and dolomite occurring both as inclusions and in the matrix were identified: group I is represented by relatively magnesium-rich calcite (Cal) (Cal<sub>I</sub>:X<sub>Mg</sub> = 0.10–0.15) and almost pure dolomite (Dol) (Dol<sub>I</sub>:X<sub>Mg</sub> = 0.47–0.48), corresponding to the Cal-Dol solvus temperatures of 707–781 °C; group II is characterized by vermicular dolomite exsolutions (Dol<sub>II</sub>:X<sub>Mg</sub> = 0.45–0.46) in Mg-rich calcite and Mg-poor calcite (Cal<sub>II</sub>:X<sub>Mg</sub> = 0.05–0.08) adjacent to Dol<sub>II</sub>, and the recorded solvus temperatures are 548–625 °C; group III is represented by nearly pure calcite (Cal<sub>III</sub>:X<sub>Mg</sub> = 0.003–0.02) and Ca-rich dolomite in the matrix (Dol<sub>III</sub>:X<sub>Mg</sub> = 0.33–0.44). Isobaric T-X(CO<sub>2</sub>) pseudosection at a peak pressure of 15 kbar in the system K<sub>2</sub>O-CaO-MgO-Al<sub>2</sub>O<sub>3</sub>-FeO-SiO<sub>2</sub>-H<sub>2</sub>O-CO<sub>2</sub> suggests that the peak fluid composition of the Thongmön forsterite marble is restricted to X(CO<sub>2</sub>) < 0.04 at T > 780 °C due to a potential infiltration event of H<sub>2</sub>O-rich fluid. Alternatively, the forsterite marble is a retrograde product subordinated to the GHS exhumation process, and its fluid composition is relatively CO<sub>2</sub>-rich (0.6 < X(CO<sub>2</sub>) < 0.8 at 5 kbar, 750 °C) at a nearly isothermal decompression stage. In either case, we suggest that the carbon flux contributed by metacarbonate rocks in an orogen setting to the global carbon cycling must be considered.



**Citation:** Chen, X.; Zhang, L.; Zhang, G.; Lü, Z. The Calcite-Dolomite Solvus Temperature and T-X(CO<sub>2</sub>) Evolution in High-Grade Impure Marble from Thongmön Area, Central Himalaya: Implications for Carbon Cycling in Orogenic Belts. *Minerals* **2022**, *12*, 724. <https://doi.org/10.3390/min12060724>

Academic Editors: Antonio Langone, Maria Pia Riccardi and Mattia Bonazzi

Received: 21 February 2022

Accepted: 2 June 2022

Published: 6 June 2022

**Publisher's Note:** MDPI stays neutral with regard to jurisdictional claims in published maps and institutional affiliations.



**Copyright:** © 2022 by the authors. Licensee MDPI, Basel, Switzerland. This article is an open access article distributed under the terms and conditions of the Creative Commons Attribution (CC BY) license (<https://creativecommons.org/licenses/by/4.0/>).

**Keywords:** impure dolomitic marble; calcite-dolomite solvus temperature; metamorphic decarbonation; the central Himalaya; carbon cycling

## 1. Introduction

Metamorphic fluid is crucial for promoting metamorphic reactions, mass transport, and partial melting [1,2], and its composition has a great impact on the element cycling in subduction zones [3–5]. In particular, metacarbonate rocks generally yield various compositions of CO<sub>2</sub>-bearing fluid due to carbonation and decarbonation reactions. In high-grade metamorphic regions, investigation of metamorphosed carbonate-bearing rocks from continental collision belts has demonstrated that fluid compositions have a great difference at different metamorphic stages, varying from nearly pure H<sub>2</sub>O to relative CO<sub>2</sub>-rich compositions [4,6–9], which may provide crucial information for the metamorphic evolution and deep carbon cycling during continental subduction and exhumation [4,6,9–11].

The carbon cycling between the biosphere, ocean, and the interior of the Earth jointly controls global climate change and furnishes our life with a livable planet [12–18]. Carbonation and decarbonation processes determine the carbon sequestration and outgassing in subduction-collision settings, e.g., the Himalaya [19–22], the North American Cordillera [23–25], the European Alps [10,26–28], the Southern Alps of New Zealand [16],

the Sivrihisar Massif, Turkey [29], and many portions of the SW Pacific Rim in Indonesia and New Guinea [30–32]. Some scholars reported that metamorphic decarbonation of metacarbonate rocks and calcic metapelites in continental collision belts could produce substantial amounts of CO<sub>2</sub> by carbonate-silicate interaction during prograde metamorphism [7–9], e.g.,  $\text{Cal} + \text{Phl} + \text{Qz} + \text{Scp} + \text{Zo} = \text{Di} + \text{Kfs} + \text{Pl} + \text{CO}_2$  [33], and the amount of carbon released from metamorphic decarbonation reactions could be three to four times higher than that consumed by silicate weathering in the Himalaya [34,35]. In addition, Guo et al. (2021) [36] inferred that a very high proportion of carbonate-rich rocks, including pelagic carbonates of Neo-Tethyan, carbonate platforms, and carbonate-rich rocks deposited in basins on the northern margin of India, was widely subducted during the Cenozoic [36,37]. The above results indicate that metamorphic CO<sub>2</sub> outgassing from the Tibetan-Himalayan greatly contributed to the global climate changes in the Cenozoic.

Nevertheless, some scholars reported relatively CO<sub>2</sub>-poor fluid composition of metacarbonate rocks during prograde metamorphism. For example, Castelli et al. (2007) [10] reported impure dolomite and calcite marbles from the UHP Brossasco-Isasca Unit (Dora-Maira Massif, western Alps), and the fluid compositions at peak conditions point to  $X(\text{CO}_2) \leq 0.0012$  and  $0.025 \leq X(\text{CO}_2) \leq 0.1$  in the dolomite marble and calcite marble, respectively. Omori et al. (1998) [6] and Liu et al. (2015) [4] both suggested that the UHP impure marbles from the Dabie Mountains have low  $X(\text{CO}_2) [= \text{CO}_2 / (\text{CO}_2 + \text{H}_2\text{O})]$  fluid compositions (0.01–0.02) at peak conditions, but these studied marbles were overprinted by an amphibolite-facies retrogression, leading to a rise in  $X(\text{CO}_2)$  of the fluid during retrograde metamorphism. In addition, Satish-Kumar et al. (2001) [31] also emphasized that retrogression from a granulite facies humite-marbles in Ambasamudram, southern India, occurred under high  $X(\text{CO}_2)$  conditions. Therefore, the evolution of fluid composition in metacarbonate rocks during retrograde metamorphism should also be considered as one of the most important factors affecting long-term global carbon cycling.

Up to now, petrological investigations and thermodynamic modeling in Thongmön area have been focused on (granulitized or retrograde) eclogites and their country-rock metapelites [38–40]; studies on high-grade metamorphic impure marble have never been reported. These impure marbles occur as lenticular intercalations or thin layers within paragneiss; thus, raising the question of whether they have experienced a similar tectonometamorphic history. Furthermore, clarifying the kinetics and types of metamorphic CO<sub>2</sub>-producing processes and fluid evolution is particularly important to understand the orogenic carbon cycling [7–9,41–45]. To shed some light on the above issues, we conducted an integrated study including petrographic observation, geochemical analysis, and thermodynamic modeling to investigate the P-T- $X_{\text{fluid}}$  evolution of the Thongmön impure marble in the central Himalaya. Moreover, we discussed the CO<sub>2</sub>-producing processes of metacarbonates in the central Himalaya and their implications for the orogenic carbon cycling.

## 2. Geological Setting

The central Himalaya, from the north to the south, is subdivided into three principal litho-tectonic units termed the Proterozoic to Eocene Tethyan Himalayan Sequence (THS) consisting of siliciclastic and carbonate rocks [46,47], the Greater Himalayan Sequence (GHS) forming a continuous belt along the east–west trending axis of the Himalaya range with a series of high-grade metamorphic rocks [48], and the Lesser Himalayan Sequence (LHS) consisting of low- to medium-grade metasedimentary rocks [49]. Almost parallel and east–west trending faults are the boundaries of these tectonic units. For example, the South Tibet Detachment System (STDS) is known as a system of normal faults between the THS above and the GHS below, and the Main Central Thrust (MCT) separates the LHS below from the GHS above (Figure 1).

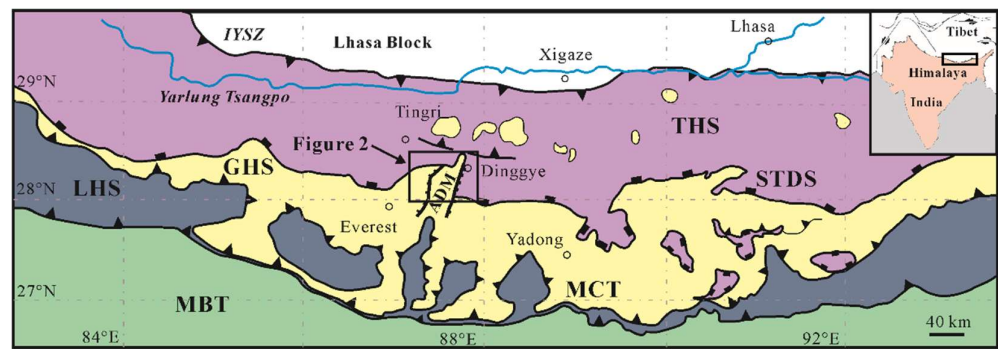


**Figure 1.** Geological sketch map of the central Himalaya showing major tectonic units (modified after Crouzet et al. (2012) [50]). The black unfilled rectangle denotes the location of Figure 2. THS: Tethyan Himalayan Sequence; GHS: Greater Himalayan Sequence; LHS: Lesser Himalayan Sequence; STDS: South Tibet Detachment System; MCT: Main Central Thrust; MBT: Main Boundary Thrust; ADM: Ama Drime Massif.

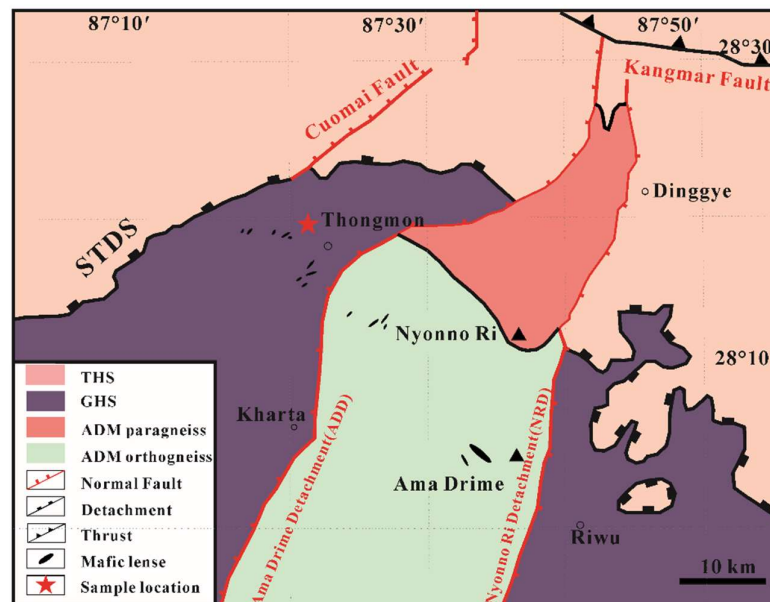


**Figure 2.** Simplified geological map of Ama Drime massif with sample location marked by a red star (modified after Li et al. (2019) [39]). Abbreviations are as in Figure 1.

The Ama Drime is a prominent N-S striking dome separated from the GHS by two opposite-dipping shear zones, the western margin Ama Drime Detachment (ADD) and the eastern margin Nyönno Ri Detachment (NRD). The western ADD is described as a 100–300 m-thick normal-sense detachment system and primarily consists of metacarbonate rocks and quartzite [51], while the eastern NRD offsets the position of the STDS right-laterally [52]. To the south of the ADM, the GHS can be divided into the Upper and the Lower Greater Himalayan Sequence termed as the UGHS and the LGHS, respectively [53]. The UGHS is mainly composed of paragneisses which were widely intruded by the Miocene leucogranite [54]. The LGHS mostly consists of strongly deformed metapelites and orthogneiss rocks with local partial melting at the early stage of retrograde metamorphism. After the anatexis, penetrative ductile shear displacements and foldings were developed [55].

The Thongmön outcrop generally comprises well-foliated metapelite with minor magmatic augen gneiss, graphitic schist, marble, and calc-silicate, and mafic pods enclosed within metapelite were also found [38]. Cottle et al. (2009) [38] suggested that the Thongmön metapelites, as well as enclosed mafic granulite, have undergone a high-temperature

retrograde overprint during isothermal exhumation, making it difficult to retrieve earlier metamorphic P-T conditions, and that the Fe-Mg garnet-biotite exchange thermometry combined with THERMOCALC calculation on the Thongmön metapelitic gneiss gave a re-equilibration condition of  $\sim 750$  °C at 5 kbar. Nevertheless, well-preserved eclogites [39] and granulitized eclogite lenses [56] within well-foliated garnet-bearing gneiss have been investigated recently in terms of their metamorphic history and evolution of the P-T path. Li et al. (2019) [39] proposed that the peak condition of the Thongmön eclogites proceeded at  $>21$  kbar,  $>750$  °C in the Miocene. In addition, a recent study documented that metapelitic rocks in the Thongmön area experienced HP granulite-facies metamorphism and then anatexis during exhumation [40]. The metamorphic conditions of these anatectic metapelites, hosting layers and lenses of (retrograde) eclogites and impure marbles ranging in thickness from several to hundreds of meters, have been estimated in the range of 13–16 kbar, 740–760 °C during prograde metamorphism and at about 13–14 kbar, 820–840 °C during a near isobaric heating stage followed by a heating decompression to 10–11 kbar,  $>860$  °C [40].

### 3. Sample Description

Several samples of impure marble from Thongmön (Figure 2) in the GHS of the central Himalayas were collected. These metacarbonates are well exposed and strongly deformed due to simultaneously or later structural folding and thrusting activities. The metapelitic rocks account for  $\sim 90\%$  of the unit volume; metacarbonate layers and lenses are on the order of 0.5- up to 10-m-thick. Occurring as distinct grey-whitish intercalations or lenses within the metapelites in Thongmön, impure marbles are very easy to recognize and could have gone through the same metamorphic evolution as the metapelites. According to the types and relative contents of silicate minerals in metacarbonates, these impure marbles were classified as forsterite-marble, diopside-marble, and tremolite-marble. The assemblage dolomite + calcite + forsterite + spinel + diopside + phlogopite + apatite  $\pm$  rutile (titanite) is representative of forsterite-marble. Diopside-marble consists of calcite, quartz, clinopyroxene, calcic plagioclase, K-feldspar, apatite, and rutile (titanite). Tremolite-marble contains a similar mineral assemblage as the diopside-marble but without clinopyroxene. Tremolite-marble is generally considered a retrograde product of diopside-marble [4,57]. These different mineral assemblages reflect different bulk compositions rather than the differences in the equilibration P-T conditions [58]. This study focuses on the forsterite marble with the aim of discussing the metamorphic decarbonation reactions and fluid evolution.

The forsterite-marble (sample DR18–55) was collected from the Thongmön area (Xigaze, China), central Himalaya, and appears as massive and banded rocks within the strongly deformed metapelites (Figure 3). The sample location is a few kilometers southwest away from that of Li et al. (2019, 2021) [39,40]. The Thongmön forsterite-marble mainly consists of calcite, dolomite, forsterite, spinel and minor phlogopite, clinohumite, and diopside. Calcite (Cal) is the most abundant carbonate in the forsterite-marble and ranges from 10 to 50  $\mu\text{m}$  in size (Figure 4). Under the microscope, some domains of calcite appear cloudy due to the presence of abundant and irregular fine-grained dolomite exsolutions (Figure 5). However, some calcite grains in the matrix almost contain no dolomite inclusions or exsolutions (Figure 5a,b). Pure Mg-calcite domains are rare. Veinlets of almost pure calcite ( $X_{\text{Mg}} < 0.003$ ) can be found not only along silicate boundaries but also crosscutting some grains of the matrix calcite and dolomite (Figure 4a,c). In addition, rounded calcite inclusions, generally 5–20  $\mu\text{m}$ , also occur in spinel, phlogopite, and forsterite (Figures 4c–f and 5a,b).

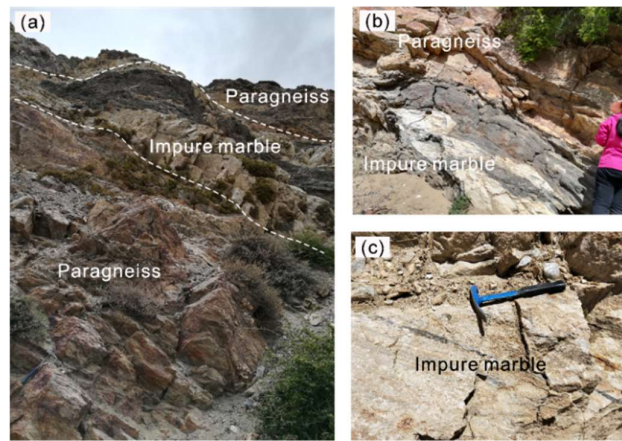


**Figure 3.** Outcrops of impure marble and surrounding paragneiss in the Thongmön area. (a,b) Impure marble lenses occur within the paragneiss; (c) impure marble with preserved sedimentary beddings and darker silicate impurities.

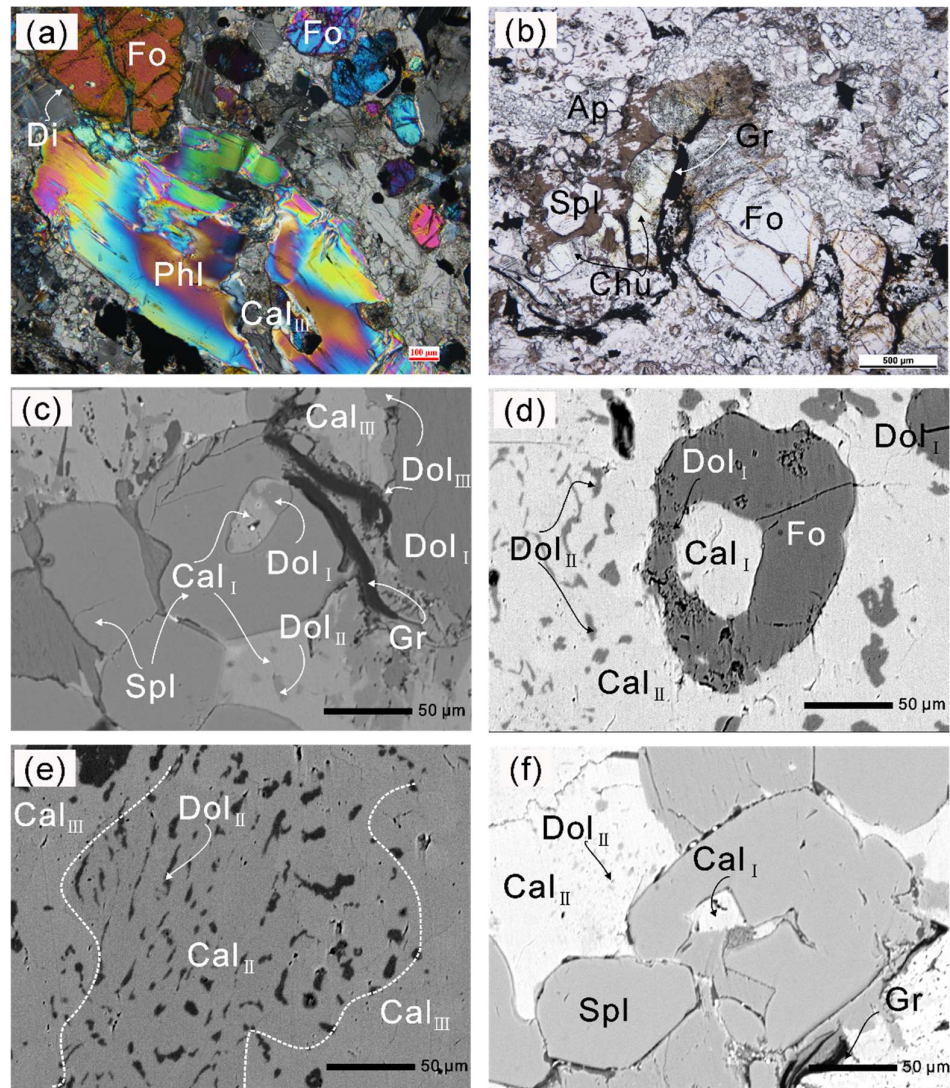


**Figure 4.** Photomicrographs and BSE (back-scattered electron) images of the Thongmön impure marbles. (a) A thin rim of diopside surrounds forsterite porphyroblast which is crosscut by later tiny

serpentine veins; phlogopite is crosscut by an almost pure calcite vein ( $Cal_{III}$ ) (crossed polarized light, XPL); (b) irregular pale yellow tabular-shaped clinohumite grains occur adjacent to forsterite (plane-polarized light, PPL); (c) Mg-calcite + dolomite polyphase inclusions in spinel indicate a primary aragonite + dolomite assemblage, and late calcite ( $Cal_{III}$ ) replaces the matrix dolomite grain ( $Dol_I + Dol_{II}$ ), producing the more Ca-rich dolomite ( $Dol_{II}$ ); (d) forsterite contains Mg-calcite + dolomite polyphase inclusions, and wormy dolomite ( $Dol_{II}$ ) exsolutions were observed in the matrix calcite ( $Cal_{II}$ ); (e) darker dolomite ( $Dol_{II}$ ) exsolutions in the Mg-poor calcite ( $Cal_{II}$ ) that is altered by the brighter almost pure calcite ( $Cal_{III}$ ); (f) Mg-calcite ( $Cal_I$ ) is captured during the formation of spinel; spinel coexists with Mg-poor calcite ( $Cal_{II}$ ) that contains wormy dolomite exsolutions. The mineral abbreviations used in the text, figures, and tables are in accordance with [59].

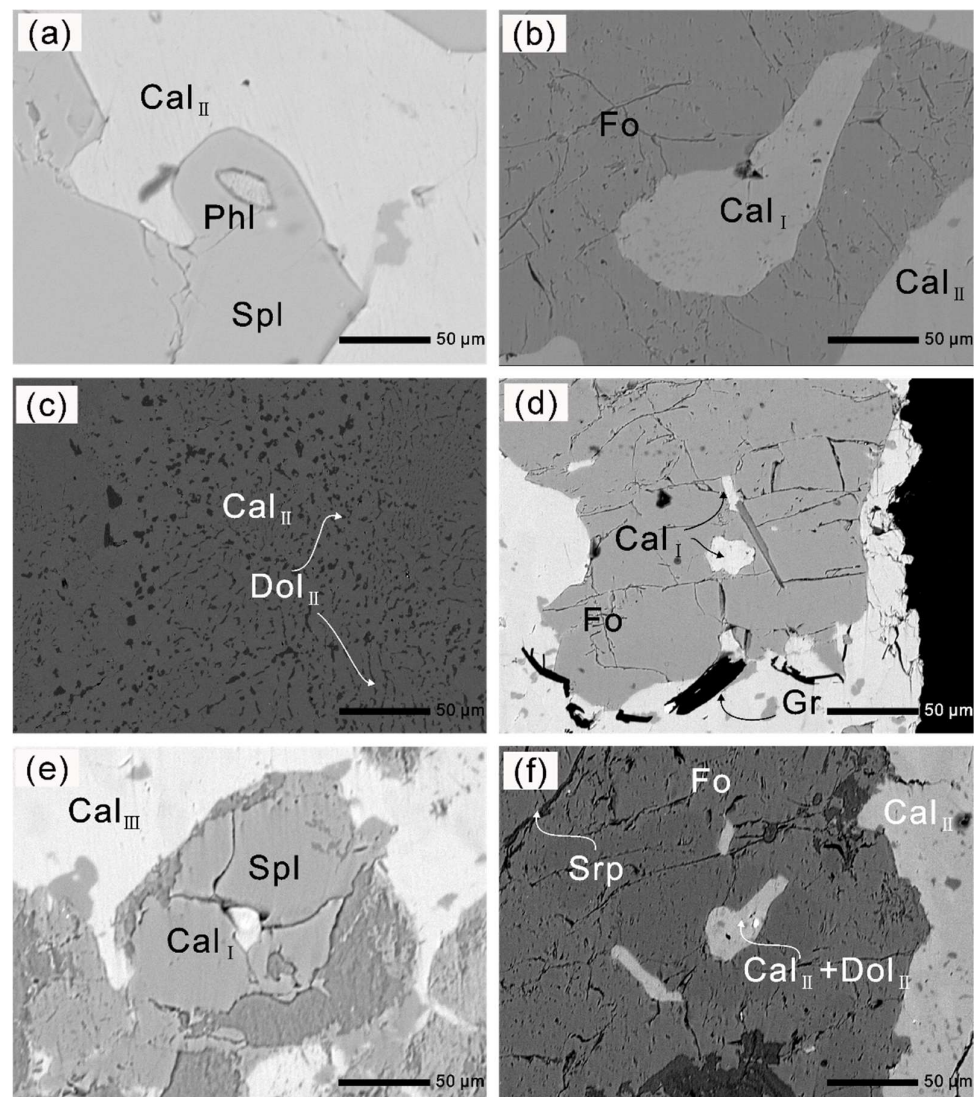


**Figure 5.** (a) Phlogopite inclusion in spinel; (b) forsterite contains a Mg-calcite inclusion ( $Cal_I$ ); (c) relatively homogeneous dolomite ( $Dol_{II}$ ) exsolved from Mg-calcite in the matrix, and the domains adjacent to dolomite ( $Dol_{II}$ ) become Mg-poor calcite ( $Cal_{II}$ ); (d) irregular oval- and rod-shaped calcite inclusions with lower aspect ratios in forsterite; (e) spinel with Mg-calcite ( $Cal_I$ ) inclusion is replaced by a very fine-grained aggregate of Mg-, Al-rich hydroxides during a late stage of metamorphic history; (f) partly serpentinized forsterite contains Mg-calcite with lower aspect ratios and Mg-calcite + dolomite polyphase inclusions.

Dolomite (Dol) occurs both as exsolutions (Figure 4d) and polyphase inclusions together with calcite (Figure 4c) in forsterite and spinel. Vermicular or wormy dolomite

lamellae and coarser dolomite exsolutions were also commonly found in the matrix calcite. In some cases, the matrix dolomite is crosscut by the veinlets of Mg-poor calcite or almost pure calcite along the cracks and grain margins (Figure 4c). The irregular contact boundaries between calcite and dolomite indicate a reaction relationship (see Section 6.1). (Mg-)calcite + dolomite polyphase inclusions in spinel and forsterite suggest the preliminary existence of aragonite during prograde metamorphism [58,60].

Spinel (Spl) is colorless, rounded in shape, and 10–50  $\mu\text{m}$  in size. Some spinel contains polyphase inclusions. Spinel is replaced by calcite and a very fine-grained aggregate of Mg- and Al-rich hydroxides during a late stage of metamorphic history (Figure 5e). In most cases, forsterite is well preserved in the matrix in contact with dolomite, calcite, and other silicates, but a few forsterite grains are partly replaced by thin veins of serpentine, suggesting that some hydration reaction occurred during retrograde metamorphism (Figure 5f). Spinel, dolomite, and calcite can also be found as inclusions in forsterites (Figures 4d and 5b,e). Phlogopite (Phl) is common both in the matrix and as inclusions (Figures 4a and 5a). In addition, phlogopite inclusions were found in zircon and spinel (Figures 5a and 6). Diopside (Di) is very rare in most forsterite-bearing impure marbles and commonly occurs as a corona surrounding forsterite (Figure 4a). Clinohumite occurs as irregular granular- to tabular-shaped grains and is colorless to pale yellow (Figure 4b), indicating its low  $\text{TiO}_2$  contents.

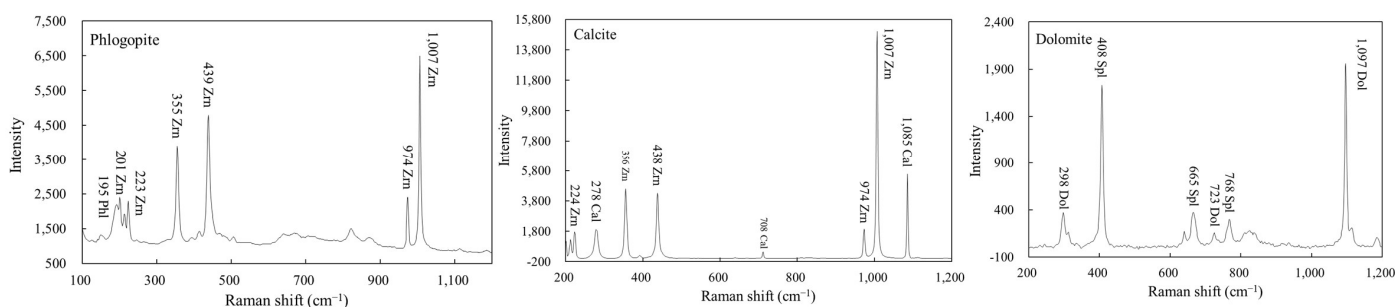


**Figure 6.** Micro-Raman spectra of calcite and phlogopite inclusions in zircon, and dolomite inclusion in spinel.

#### 4. Analytical Methods

Whole-rock major element compositions were determined by X-ray fluorescence spectrometry (XRF, PrimusII, Rigaku, Osaka, Japan) and inductively coupled plasma-mass spectrometry (ICP-MS, Agilent 7700e, Wuhan Sample Solution Analytical Technology Co., Ltd., Wuhan, China). Mineral composition analysis and back-scattered electron (BSE) imaging were performed with an electron microprobe (EMP, JEOL JAX-8100) at the Key Laboratory of Orogenic Belts and Crustal Evolution, Peking University, China. The analyses were operated in wavelength dispersion mode (WDS) with a 10 nA beam current and a 15 kV accelerating voltage. A minimum beam diameter of 1–3  $\mu\text{m}$  and a defocused beam of  $\sim 10 \mu\text{m}$  were used for silicate and carbonate minerals, respectively. To reduce the measurement error and improve the data reproducibility, carbonates containing  $<10 \mu\text{m}$  exsolution lamellae were measured using a broad beam of diameter 50  $\mu\text{m}$  for obtaining the average chemical composition. Fluorine contents in clinohumite and phlogopite were also analyzed under 15 kV accelerating voltage and 40 nA beam current conditions with a beam diameter of  $\sim 20 \mu\text{m}$ . SPI standards were utilized and raw data were reduced with the Phi-Rho-Z (PRZ) correction [61].

Raman analysis of mineral inclusions in zircon and other minerals was performed on a Renishaw-RW 1000 Raman microprobe adopting the 514.5 nm line of an Ar-ion laser at the School of Earth and Space Sciences, Peking University. The analytical procedures followed the description in [62]. The accumulation time varied from 5 to 10 s and the laser spot size was focused to 2  $\mu\text{m}$ . The estimated spectral resolution was  $1.0 \text{ cm}^{-1}$ , and the spectrum reproducibility is better than  $0.05 \text{ cm}^{-1}$ . Calibration was conducted using synthetic silicon

and spectra were fitted using the Peakfit software (v4.04, Aisn Software Inc., Wilmington, DE, USA).

### 5. Results

#### 5.1. Mineral Chemistry

Some domains of calcite show textural and chemical heterogeneity with  $0.05 < X_{Mg}$  ( $Mg/(Ca + Mg + Fe) < 0.08$  (Table 1). However, some calcite grains display more homogeneous chemical compositions with  $0.10 < X_{Mg} < 0.15$ . Almost pure calcite ( $X_{Mg} < 0.003$ ) can also be found. Generally, the FeO and MnO contents in calcite are below the detection limits.

**Table 1.** Representative microprobe analyses of matrix carbonates and carbonate inclusions in silicates and oxides from the Thongmön impure marbles.

Textural Position	Cal <sub>I</sub>						Cal <sub>I</sub>			
	In Fo	In Fo	In Phl	In Fo	In Fo	In Spl	In Matrix			
CaO (wt%)	50.39	50.71	52.23	50.86	50.91	54.35	53.90	62.60	44.20	52.69
MgO	5.98	5.55	4.87	5.79	5.12	7.06	4.16	5.22	3.70	4.32
FeO	0.07	0.03	0.11	0.04	0.12	0.14	0.03	0.18	0.10	0.09
Total	56.44	56.29	57.21	56.69	56.15	61.55	58.09	68.00	48.00	57.10
Ca (a.p.f.u)	1.71	1.73	1.77	1.72	1.75	1.69	1.80	1.79	1.79	1.79
Mg	0.28	0.26	0.23	0.27	0.25	0.31	0.19	0.21	0.21	0.20
Fe	0.00	0.00	0.00	0.00	0.00	0.00	0.00	0.00	0.00	0.00
$X_{Mg}$ <sup>1</sup>	0.142	0.132	0.115	0.137	0.123	0.153	0.097	0.104	0.104	0.102
T (°C) <sup>2</sup>	760	742	707	750	724	781	667	683	684	680
	Cal <sub>II</sub>						Cal <sub>III</sub>			
	in matrix						in matrix			
CaO	54.04	53.09	54.19	53.27	53.02	54.52	53.29	53.22	54.62	55.16
MgO	2.29	2.34	2.49	2.51	3.33	2.38	3.33	3.30	0.05	0.12
FeO	0.00	0.08	0.06	0.09	0.01	0.01	0.05	0.04	0.00	0.03
Total	56.33	55.51	56.74	55.87	56.36	56.91	56.67	56.56	54.67	55.31
Ca	1.89	1.88	1.88	1.87	1.84	1.88	1.84	1.84	2.00	1.99
Mg	0.11	0.12	0.12	0.12	0.16	0.11	0.16	0.16	0.00	0.01
Fe	0.00	0.00	0.00	0.00	0.00	0.00	0.00	0.00	0.00	0.00
$X_{Mg}$	0.056	0.058	0.060	0.062	0.080	0.057	0.080	0.079	0.002	0.003
T (°C)	548	556	564	569	625	554	625	622		
	Dol <sub>I</sub>	Dol <sub>I</sub>	Dol <sub>II</sub>	Dol <sub>III</sub>	Dol <sub>III</sub>	Dol <sub>III</sub>				
CaO	32.05	32.38	35.11	35.28	35.47	32.98	32.46	37.26	37.79	42.56
MgO	21.54	21.30	20.30	20.69	21.71	20.54	20.17	20.98	18.87	15.06
FeO	0.17	0.22	0.22	0.18	0.22	0.19	0.19	0.17	0.18	0.12
Total	53.76	53.90	55.63	56.15	57.40	53.71	52.82	58.41	56.84	57.74
Ca	1.03	1.04	1.10	1.10	1.08	1.07	1.07	1.12	1.18	1.34
Mg	0.96	0.95	0.89	0.89	0.92	0.93	0.92	0.88	0.82	0.66
Fe	0.00	0.01	0.01	0.00	0.01	0.01	0.01	0.00	0.00	0.00
$X_{Mg}$	0.48	0.48	0.45	0.45	0.46	0.46	0.46	0.44	0.41	0.33

<sup>1</sup>  $X_{Mg} = Mg/(Ca + Mg + Fe)$ ; <sup>2</sup> temperatures are calculated by the calcite-dolomite solvus geothermometer from Anovitz and Essene (1987) [65] and Hermann et al. (2016) [66]. Structural formulae are calculated based on  $\Sigma$  cations = 2.

The vermicular dolomite inclusions in calcite generally have the  $X_{Mg}$  values of 0.45–0.46. Matrix dolomite ( $X_{Mg} = 0.48$ ) (Table 1) rarely contains tiny calcite inclusions which are too small to be analyzed precisely (Figure 4d). Some dolomite grains display higher Ca contents or lower Mg contents ( $X_{Mg} = 0.33$ – $0.44$ ) compared with nearly pure dolomite ( $X_{Mg} = 0.48$ ) in the matrix. Although FeO contents are generally negligible in dolomite and calcite, dolomite contains slightly higher FeO content than calcite.

An almost pure Mg-Al spinel with the Mg/(Mg + Fe) ratio of 0.99 hosts Mg-calcite and dolomite inclusions (Figure 4c). Forsterite (10–100 µm) is generally irregular in shape with >0.98 forsterite (Fo) contents (Table 2).

Phlogopite grains in the matrix usually contain Mg-calcite inclusions with a maximum  $X_{Mg}$  value of 0.115. The Mg/(Mg + Fe) ratio in phlogopite is generally >0.99 and the TiO<sub>2</sub> content can be up to 0.57 wt%.

Clinopyroxene is nearly pure diopside. Clinohumite (Chu) occurs as granoblastic crystals associated with forsterite and spinel. The TiO<sub>2</sub> contents of clinohumite range from 1.54 to 1.96 wt% and the fluorine contents range from 1.68 to 2.18 wt% (Table 2). A certain amount of fluorine can stabilize the humite group minerals to higher temperatures [63,64].

**Table 2.** Microprobe analyses of silicates and oxides in the Thongmön impure marbles.

	Fo	Fo	Fo	Chu	Chu	Chu	Phl	Phl	Phl	Spl	Spl
SiO <sub>2</sub> (wt%)	41.06	41.97	41.82	39.02	39.08	39.07	42.83	40.52	40.46	0.01	0.02
TiO <sub>2</sub>	0.00	0.00	0.00	0.64	0.48	0.53	0.57	0.07	0.57	0.00	0.03
Al <sub>2</sub> O <sub>3</sub>	0.02	0.03	0.02	0.02	0.00	0.02	13.57	15.9	14.62	69.89	70.33
FeO	1.40	1.50	1.42	0.97	1.00	0.86	0.29	0.32	0.26	1.30	1.34
MnO	0.00	0.01	0.06	0.06	0.04	0.07	0.04	0.02	0.01	0.00	0.06
MgO	57.55	56.78	55.93	58.08	58.65	57.88	27.58	26.74	25.82	25.87	26.37
CaO	0.08	0.03	0.00	0.02	0.02	0.05	0.54	0.02	0.18	0.19	0.04
Na <sub>2</sub> O	0.00	0.00	0.02	0.00	0.00	0.00	0.42	0.26	0.19	0.00	0.00
K <sub>2</sub> O	0.02	0.00	0.00	0.01	0.01	0.00	9.3	9.63	10.13	0.04	0.00
F	0.00	0.00	0.00	2.21	2.29	2.40	0.74	0.87	2.21	0.07	0.06
F=O	0.00	0.00	0.00	−0.93	−0.99	−1.01	−0.31	−0.37	−0.93	−0.03	−0.03
Total	100.23	100.29	99.27	100.09	99.59	99.87	95.57	94.02	93.52	97.34	98.22
Si (a.p.f.u)	1.00	1.00	1.00	3.98	3.97	3.99	2.97	2.86	2.91	0.00	0.00
Ti	0.00	0.00	0.00	0.05	0.04	0.04	0.03	0.00	0.03	0.00	0.00
Al	0.00	0.00	0.00	0.00	0.00	0.00	1.11	1.32	1.24	2.02	2.01
Fe <sup>2+</sup>	0.02	0.03	0.03	0.08	0.09	0.07	0.01	0.02	0.01	0.03	0.03
Mn	0.00	0.00	0.00	0.00	0.00	0.00	0.00	0.00	0.00	0.00	0.00
Mg	1.97	1.98	1.96	8.84	8.89	8.83	2.85	2.81	2.76	0.94	0.95
Ca	0.00	0.00	0.00	0.01	0.00	0.01	0.04	0.03	0.01	0.01	0.00
Na	0.00	0.00	0.00	0.01	0.00	0.00	0.06	0.04	0.03	0.00	0.00
K	0.00	0.00	0.00	0.01	0.00	0.00	0.82	0.87	0.93	0.00	0.00
Sum <sup>1</sup>	2.99	3.01	2.99	12.97	12.99	12.96	7.9	7.93	7.92	2.99	2.99
F	0.00	0.00	0.00	0.71	0.74	0.78	0.16	0.19	0.5	0.01	0.01
$X_{Mg}$ <sup>2</sup>	0.99	0.99	0.99	0.99	0.99	0.99	1.00	0.99	0.995	0.97	0.97

<sup>1</sup> Structural formulae are calculated based on 3, 13, 8, and 3 cations for Fo, Phl, Chu, and Spl, respectively.

<sup>2</sup>  $X_{Mg} = Mg/(Mg + Fe)$ .

## 5.2. Calcite-Dolomite Solvus Geothermometer

The calcite-dolomite solvus thermometer is a widely used geothermometer for marbles [65–67]. Anovitz and Essene (1987) [65] provided an empirical calibration of the solvus thermometer in the range of 473–1173 K with ±10 °C uncertainty. Recently, Hermann et al. (2016) [66] performed an experimental constraint on the reaction of dolomite + aragonite to Mg-calcite at 2–6.5 GPa, 660–940 °C, emphasizing the important role of an experimental calibration of this reaction in interpreting subducted impure marbles. This thermometer has been applied to inclusions that are located far from the margin of the host minerals and not crosscut by late-stage calcite or serpentinized veins [65].

The  $X_{Mg}$  (Mg/(Mg + Ca + Fe)) compositions of Mg-calcite inclusions (Cal<sub>I</sub>) in spinel, forsterite, and phlogopite range from 0.097 to 0.153, corresponding to the solvus temperatures of 707–781 °C, which is at least 100 °C higher than the recorded temperature of the matrix Mg-calcite (Cal<sub>I</sub>). The  $X_{Mg}$  compositions of Mg-poor calcite in the matrix (Cal<sub>II</sub>) are from 0.056 to 0.080, corresponding to the solvus temperature of 548–625 °C. Calcite grains (Cal<sub>III</sub>) with lower  $X_{Mg}$  values (0.002–0.02) imply that the solvus temperatures are below 400 °C, which may be attributed to later retrograde metamorphism. Thus, the

compositions of these carbonates cannot be used to calculate and evaluate the metamorphic temperatures. Pure calcite inclusions in spinel and forsterite were not found, but Mg-calcite and polyphase dolomite + Mg-calcite inclusions were included in spinel. An Mg-calcite inclusion ( $X_{Mg} = 0.153$ ) in spinel constrains a minimum temperature of 781 °C for the growth of this spinel grain. This value is the highest temperature recorded by Mg-calcite composition in the Thongmön impure marble.

We analyzed the compositions of carbonate inclusions in forsterite without serpentinization to undertake a further evaluation of temperature. The  $X_{Mg}$  values of monophase Mg-calcite and composite carbonate inclusions consisting of dolomite and Mg-calcite inclusions in forsterite are from 0.12 to 0.14, corresponding to the calcite-dolomite solvus temperature of 720–760 °C, which is lower than that of the maximum 781 °C recorded in spinel. The composition of carbonate inclusions in forsterite indicates that the temperature was at least >720 °C during forsterite growth. Calcite inclusion with  $X_{Mg} = 0.115$  in phlogopite gives the corresponding solvus temperature of 707 °C, which is slightly lower than that recorded in spinel and forsterite. The lower temperature record was possibly influenced by the infiltration of later external fluids along phlogopite cleavage.

Notably, various compositions, shapes, and sizes of carbonate inclusions possibly recorded different temperatures at different metamorphic stages. Thus, to obtain the peak metamorphic temperatures, it is necessary to carefully select those characteristic carbonate inclusions that have homogenous and unmixing features. In this study, the chemical composition of carbonate does not show distinct zoning patterns in terms of calcium and magnesium. The absence of zoning features can be attributed to the relatively higher temperature or/and longer crustal residence time of impure marble in the Tibetan-Himalayan orogenic belt. Experimental work on the cation diffusion in carbonate minerals indicates that the chemical heterogeneities will be erased by the thermal diffusion if heating temperatures are high enough and/or the duration is long [68].

### 5.3. Phase Diagram Modeling

P/T-X(CO<sub>2</sub>) phase diagrams in the CaO-K<sub>2</sub>O-FeO-MgO-Al<sub>2</sub>O<sub>3</sub>-SiO<sub>2</sub>-H<sub>2</sub>O-CO<sub>2</sub> (CKFMAS-HC) system were calculated using *Perple\_X* (version 6.7.7, June 2018) [69,70] with the internally consistent thermodynamic dataset from [71] and adopting the bulk composition of DR18-55. Ferric iron was neglected due to its very low contents in the analyzed minerals and the absence of Fe<sup>3+</sup>-rich oxides. The calculation of P/T-X(CO<sub>2</sub>) pseudosection in the CKFMAS-HC system adopted the following solid solution models: dolomite Do(HP) [71], garnet Gt(HP) [71], clinopyroxene Cpx(HP) [71], biotite Bio(TCC) [72], olivine O(HP) [71], spinel Sp(HP) [71], amphibole Amph (DHP) [73], calcite Cc(AE) [65], and clinohumite Chu, ideal model [71]. The binary H<sub>2</sub>O-CO<sub>2</sub> fluid was considered as a saturated fluid phase. Muscovite and K-feldspar were treated as pure end-members.

We constructed P/T-X(CO<sub>2</sub>) pseudosections for impure marble in the H<sub>2</sub>O-CO<sub>2</sub> saturated system; thus, hydrous phases in equilibria can be calculated and shown in such a phase diagram. The reasons for constructing such a phase diagram were (1) to illustrate a series of metamorphic decarbonation reactions occurring during peak and nearly isothermal decompression metamorphism and (2) to constrain the fluid evolution at certain P-T conditions of the Thongmön impure forsterite marble. The fluid evolution can be qualitatively constrained by isobaric P/T-X(CO<sub>2</sub>) pseudosections. Fixed pressures of 15 and 5 kbar were used for T-X(CO<sub>2</sub>) pseudosection calculation, following the previous estimate of pressure on metapelites at peak and retrograde stages which are spatially related to the impure marble [38,40].

The T-X(CO<sub>2</sub>) pseudosection at 15 kbar (Figure 7) is dominated by large tri- and four-variant fields, with few narrow two-variant fields. Calcite/aragonite is always stable in the whole region of interest. Dolomite is absent in Bt + Spl + Chu + Cal, Bt + Fo + Spl + Chu + Cal, and Bt + Fo + Spl + Cpx + Cal stability fields. Regardless of the composition of the fluid, muscovite can be stable below 700 °C, whereas biotite appears at higher temperatures on the relatively low X(CO<sub>2</sub>) side. Spinel can only be found in a

narrow stability field at  $X(\text{CO}_2) < 0.2$ , and the stability field of clinohumite is limited to the extremely  $\text{H}_2\text{O}$ -rich side. Forsterite together with biotite, dolomite, spinel, and calcite occur at  $650\text{ }^\circ\text{C} < T < 850\text{ }^\circ\text{C}$  and within the field of  $X(\text{CO}_2) < 0.12$ . Diopside can be found on the  $\text{CO}_2$ -poor side at lower temperatures and on the  $\text{CO}_2$ -rich side at higher temperatures. In addition, in order to trace the fluid evolution during isothermal exhumation, we also constructed the  $T$ - $X(\text{CO}_2)$  pseudosection at a fixed pressure of 5 kbar and  $P$ - $X(\text{CO}_2)$  pseudosection at a fixed temperature of  $750\text{ }^\circ\text{C}$  (Figure 8). The  $\text{Bt} + \text{Dol} + \text{Fo} + \text{Spl} + \text{Cal}$  stability field at 5 kbar extends to be wider than that at 15 kbar. The  $X(\text{CO}_2)$  of the fluid in the Thongmön impure marble can reach up to 0.8 at 5 kbar,  $750\text{ }^\circ\text{C}$ . Similarly, the  $P$ - $X(\text{CO}_2)$  diagram at  $750\text{ }^\circ\text{C}$  indicates that the fluid compositions evolve to be  $\text{CO}_2$ -richer during isothermal exhumation.

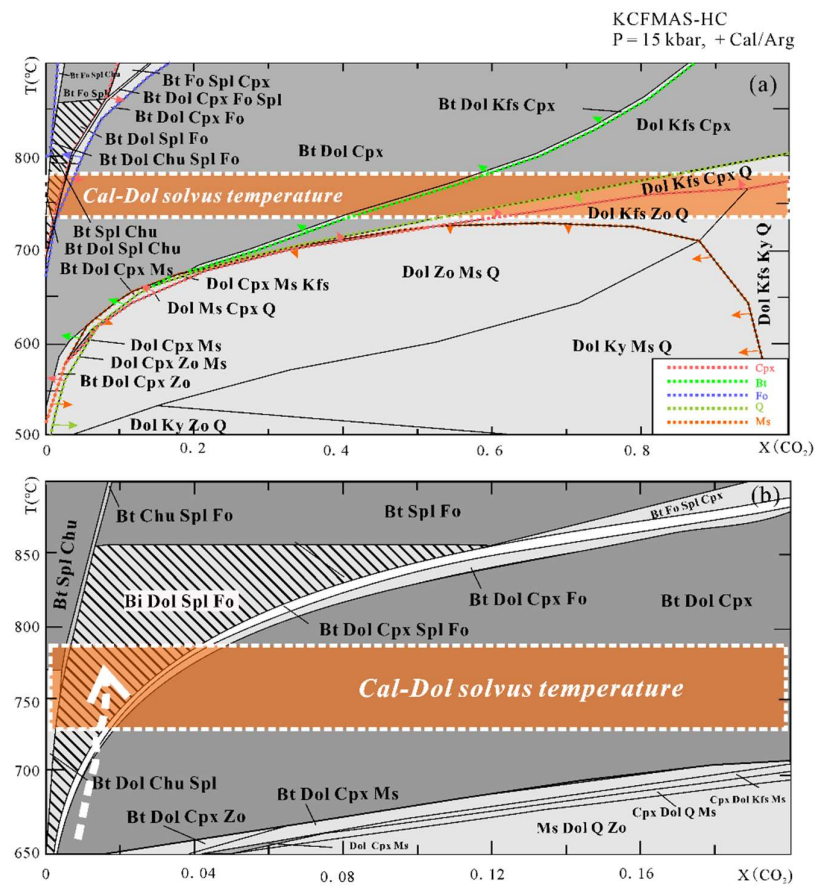


**Figure 7.** (a)  $T$ - $X(\text{CO}_2)$  pseudosections at 15 kbar ( $X(\text{CO}_2) = 0$ –1) for the Thongmön impure marble in the system CKFMAS-HC (the modeling oxide compositions are as follows:  $\text{SiO}_2 = 11.74$ ,  $\text{MgO} = 21.42$ ,  $\text{Al}_2\text{O}_3 = 1.29$ ,  $\text{CaO} = 31.79$ ,  $\text{FeO} = 0.36$ ,  $\text{K}_2\text{O} = 0.15$  from the XRF analysis, in wt%). Light- and dark-grey fields are tri- and quadri-variant fields, respectively. Different color dashed lines with arrows are phase-in boundaries. The mineral assemblages in the shaded field are predicted by the  $T$ - $X(\text{CO}_2)$  pseudosection and also observed as inclusions in the metamorphic zircons. White dashed lines with orange filled band represent the range of peak temperature at 15 kbar evaluated by the calcite-dolomite solvus thermometer from Anovitz and Essene (1987) [65] and Hermann et al. (2016) [66]; (b) the same  $T$ - $X(\text{CO}_2)$  pseudosection as (a) but with a narrower fluid range from pure  $\text{H}_2\text{O}$  to  $X(\text{CO}_2) = 0.2$ . The white dashed arrow points to the internally buffered  $T$ - $X(\text{CO}_2)$  path compatible with both the observed peak assemblage and the corresponding decarbonation Reactions (2)–(4). See more details in the text.

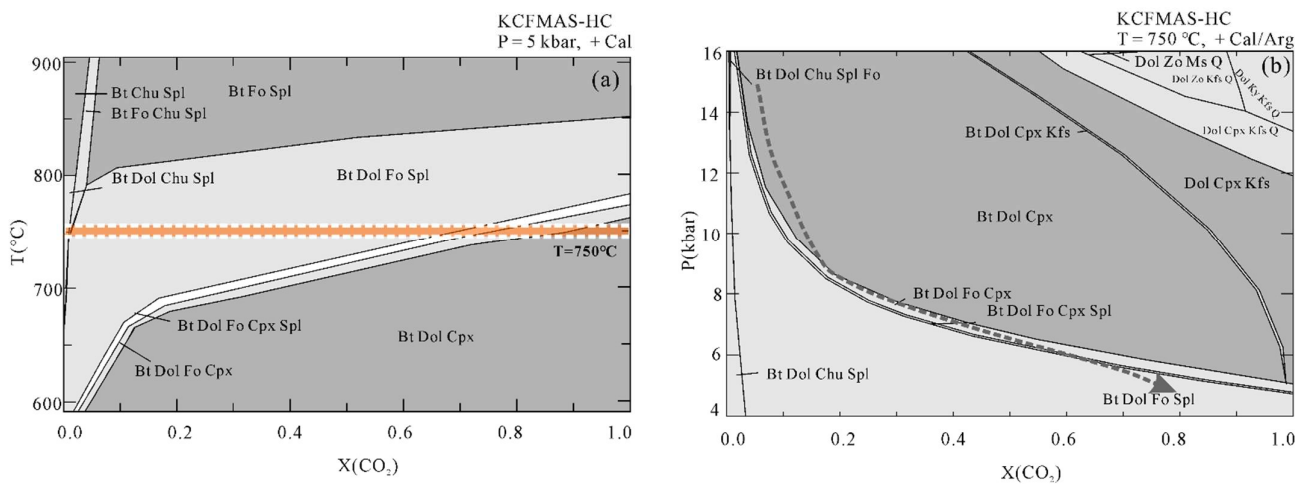


**Figure 8.** (a) T- $X(\text{CO}_2)$  pseudosection at 5 kbar and (b) P- $X(\text{CO}_2)$  pseudosection at 750 °C. The thick dashed line indicates a possible P- $X(\text{CO}_2)$  path showing the fluid evolution during isothermal exhumation.

## 6. Discussion

### 6.1. Different Generations of Carbonates and Mineral Reaction History in the Impure Marble

A common method of retrieving the P-T history of metamorphic rocks is to gather information from the well-preserved inclusions in refractory minerals and from the metamorphic reaction textures [74,75]. This method is categorically evidenced by the description of coesite and diamond inclusions in felsic granulite formed at UHP conditions [76]. Carbonate inclusions in impure marble, which is less prone to be influenced by late retrograde metamorphism, can not only provide crucial information on the temperature of formation of the host minerals [4,58,66] but also constrain the mineral reaction history. Thus, carbonate inclusions are extraordinary candidates for extracting metamorphic evolution information on high-grade metamorphic marbles.

Three generations of calcite can be recognized. The first generation contains the inclusion-free Mg-calcite with  $0.10 < X_{\text{Mg}} < 0.15$  ( $\text{Cal}_I$ ) coexisting with pure matrix dolomite, forsterite, spinel, and phlogopite (Figure 9a). The second generation is documented by the exsolution of dolomite from the primary homogenous Mg-calcite (Figure 9b). The lath-shape and vermicular intergrowths of dolomite in Mg-poor calcite with  $0.05 < X_{\text{Mg}} < 0.08$  ( $\text{Cal}_{II}$ ) are not uncommon in the Thongmön impure marbles. The last generation is represented by the formation of almost pure calcite with  $X_{\text{Mg}} < 0.003$  ( $\text{Cal}_{III}$ ) via an external  $\text{CO}_2$ -rich hydrous fluid flux (Figure 9c). Moreover, this hydration event also resulted in the growth of serpentine replacing forsterite. In the same way, three generations of dolomite can also be recognized (Figure 9).  $\text{Dol}_I$  ( $X_{\text{Mg}} > 0.48$ ) forms coarse grains in the matrix, and smaller grains occur as mineral inclusions. The second generation ( $\text{Dol}_{II}$ ) ( $X_{\text{Mg}} = 0.45\text{--}0.46$ ) forms fine-grained exsolutions in Mg-poor calcite ( $\text{Cal}_{II}$ ) in the matrix, showing wormy or elliptical shapes with low aspect ratios. Some  $\text{Dol}_{II}$  crystals coexist with Mg-poor calcite as polyphase inclusions within spinel and forsterite, showing tiny dolomite lamellae exsolution textures in the Mg-poor calcite host. Locally, the matrix dolomite is crosscut by the veinlets of Mg-poor calcite or almost pure calcite ( $\text{Cal}_{III}$ ) along cracks and grain margins, and it is transformed in  $\text{Dol}_{III}$  with lower Mg contents ( $X_{\text{Mg}} = 0.33\text{--}0.44$ ).

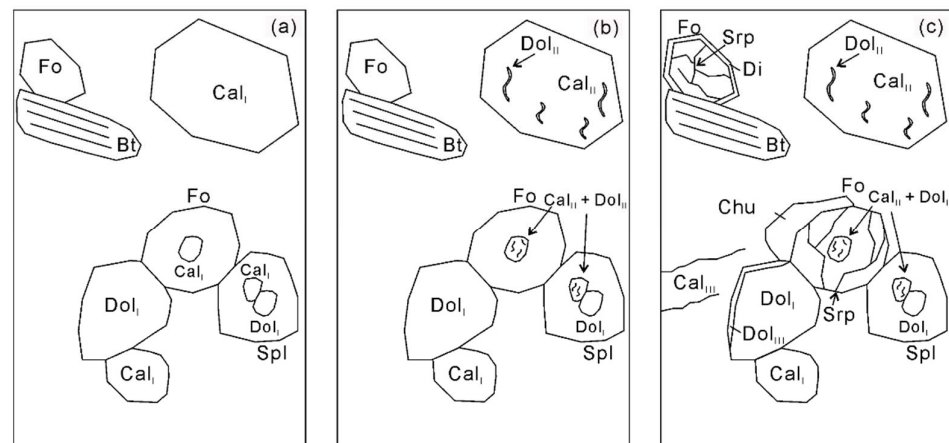
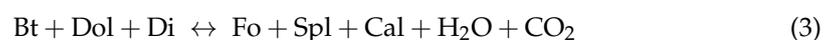
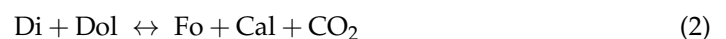


**Figure 9.** Sketch of three generations of calcite and dolomite and the mineral assemblages coexisting with them. (a) The first generation Cal<sub>I</sub> and Dol<sub>I</sub> coexist with forsterite, spinel, and phlogopite; (b) the second generation Dol<sub>II</sub> is exsolved from the primary homogenous Mg-calcite (Cal<sub>I</sub>), leading to the formation of Mg-poor calcite (Cal<sub>II</sub>); (c) the last generation Cal<sub>III</sub> and Dol<sub>III</sub> is formed via an external CO<sub>2</sub>-rich hydrous fluid flux. For more details see the text.

As outlined above, firstly, the dolomite (Dol<sub>I</sub>) and Mg-calcite (Cal<sub>I</sub>) polyphase inclusions in spinel and forsterite (Figure 4c,d) imply the existence of former aragonite during prograde metamorphism (Reaction (1)). Forsterite and calcite (Cal<sub>II</sub>) were formed by Reaction (2) in the presence of dolomite (Dol<sub>II</sub>) and diopside, but the absence of primary diopside in the matrix or as inclusions may imply that it has been exhausted during prograde metamorphism. Moreover, the thin reaction rims of dolomite and diopside around forsterite indicate that forsterite was a stable phase at peak conditions (Figure 4). Spinel and forsterite started to form more or less at the same time by Reaction (3). Notably, Reaction (3) will produce a K-rich aqueous fluid due to the absence of a K-bearing phase among the products. In the presence of an external H<sub>2</sub>O-rich fluid during exhumation, clinohumite and calcite (Cal<sub>III</sub>) were formed by Reaction (4). However, if the forsterite marble is a retrograde product of diopside marble, these decarbonation reactions can also be applied to the trace its fluid evolution.



Proyer et al. (2008) [58] proposed that clinohumite can also grow by a decarbonation reaction consuming diopside and dolomite:  $\text{Di} + \text{Dol} + \text{H}_2\text{O} \rightarrow \text{Chu} + \text{Cal} + \text{CO}_2$ . However, from petrological observation of this study, the growth of clinohumite from forsterite is testified by clinohumite rimming forsterite (Figure 4b). The high amount of fluorine in clinohumite and phlogopite indicates that an external fluorine-bearing hydrous fluid (or melt) played a crucial role in their growths. The tiny serpentinization veins through forsterite also indicate a later hydration process. However, the very low amount of clinohumite and serpentine testifies that such a process is limited.

## 6.2. Metamorphic Fluid Evolution of the Thongmön Impure Marble

We attempted to construct the P/T-X(CO<sub>2</sub>) pseudosections to evaluate the fluid composition under peak and retrograde conditions, which may provide some clues on the metamorphic evolution of impure marbles. In addition, most metamorphic reactions in metacarbonates are strongly dependent on temperature and more or less subparallel to

each other in P-T space [58]. In this case, constructing the P/T-X(CO<sub>2</sub>) diagrams is a direct attempt.

Forsterite-spinel impure marbles are typical for high-grade granulite-facies terrains such as southern India [30,31], northeastern Greece [58,60], and central Australia [77]. Rapa et al. (2017) [41] reported that the prograde growth of titanite in the calc-silicate rocks from the Nepal Himalaya (GHS) is closely associated with the substantial release of CO<sub>2</sub>. In addition, Groppo et al. (2013, 2017) [9,33] investigated the metamorphic evolution of calc-silicate rocks from the eastern Nepal Himalaya and concluded that the formation of garnet and scapolite involved simultaneous CO<sub>2</sub>-producing reactions with a relatively CO<sub>2</sub>-rich fluid composition ( $X(\text{CO}_2)_{\text{max}} = 0.44$ ) at peak conditions and that estimated metamorphic CO<sub>2</sub> flux was about  $1.1\text{--}3.4 \times 10^{10}$  mol/year. However, Castelli et al. (2007) [10] reported the impure marbles from the UHP Brossasco-Isasca Unit (Dora-Maira Massif, western Alps) and suggested that the modeled fluid compositions at peak conditions point to  $X(\text{CO}_2) \leq 0.0012$  and  $0.025 \leq X(\text{CO}_2) \leq 0.1$  in the dolomite marble and calcite marble, respectively. In addition, Proyer et al. (2008) [58] investigated the high-grade aluminous calcite-dolomite marbles from the Greek Rhodope massif and claimed that the assemblages preserved in these marbles most probably equilibrated at  $a_{\text{CO}_2} \sim 0.01$ . Similarly, in the Dabie Mountains, China, the peak fluid composition of the UHP impure marble was extremely H<sub>2</sub>O-rich with  $X(\text{CO}_2) < 0.02$  [4,6].

Forsterite-spinel impure marbles may be a product of prograde metamorphism. We take two steps to constrain the fluid composition during prograde to the peak metamorphism. Firstly, we used the mineral assemblage at peak conditions of the impure marble to outline the X(CO<sub>2</sub>) range. Combined with the petrological observation and metamorphic evolution as mentioned above, the Thongmön impure marble has a peak mineral assemblage of forsterite, spinel, calcite, dolomite, and phlogopite. Thus, it is easy to see from the T-X(CO<sub>2</sub>) diagram that the composition of peak fluid is  $X(\text{CO}_2) < 0.12$  (Figure 7a). Following this range, we applied the acquired calcite-dolomite solvus temperature to the T-X(CO<sub>2</sub>) diagram and obtained an intersection point that corresponds to an approximate fluid composition of  $X(\text{CO}_2) < 0.04$  (Figure 7b). Our modeling results thus suggest that the fluid composition of the Thongmön impure marble is relatively CO<sub>2</sub>-poor ( $X(\text{CO}_2) < 0.04$ ) at the peak stage. At such high temperatures (>750 °C), metamorphic decarbonation reactions should have been robust to produce a large amount of CO<sub>2</sub> furnishing the hydrous fluid with higher X(CO<sub>2</sub>), which is not in accordance with our modeling results and petrological observations. Thus, in this case, a weak metamorphic decarbonation process is not supported, and such high H<sub>2</sub>O contents of fluid at peak conditions may imply that the Thongmön forsterite marble experienced significant infiltration of external H<sub>2</sub>O-rich fluid, which is consistent with the results from Buick et al. (1997) and Proyer et al. (2008) [58,77].

Alternatively, forsterite-bearing marble may be formed during the decompression exhumation process. In this way, the evolution of fluid composition during isothermal exhumation gradually becomes richer in CO<sub>2</sub> (Figure 8). Specifically, the former diopside-bearing marble has a H<sub>2</sub>O-rich ( $X(\text{CO}_2) < 0.1$ ) fluid composition at the peak stage and then gets CO<sub>2</sub>-richer with the formation of forsterite by the decarbonation reaction:  $\text{Di} + \text{Dol} = \text{Fo} + \text{Cal} + \text{CO}_2$ . Due to the continuous isothermal exhumation process, the fluid composition could be partly buffered along with the producing forsterite and spinel equilibria from  $X(\text{CO}_2) = 0.2$  at ~9 kbar until the diopside is nearly exhausted at  $X(\text{CO}_2) = 0.5$  at ~7 to 6 kbar (Figure 8b). At last, it may evolve to  $0.6 < X(\text{CO}_2) < 0.8$  at 5 kbar, 750 °C assuming that the impure marble is subordinate to the retrograde evolution of the GHS [38–40]. Therefore, the decompression process results in an increase in X(CO<sub>2</sub>) of fluid during the exhumation of the Thongmön impure marble. An increase in X(CO<sub>2</sub>) of fluid in the UHP impure marbles during isothermal exhumation from the Dabie Mountains is reported by Liu et al. (2015) [4] and Omori et al. (1998) [6]. The relatively higher X(CO<sub>2</sub>) in fluid during isothermal exhumation decreased again at a late retrograde stage, which could partly be attributed to the infiltration of external aqueous fluids leading to a dilution in CO<sub>2</sub> of the fluid. The formation of serpentinite and clinohumite also testify to the occurrence of

a hydration event. In this regard, the fluid composition of the Thongmön impure marble varies greatly in the whole metamorphic evolution

### 6.3. Implications for the Carbon Cycling in Orogenic Belts

Global carbon cycling plays an important role in controlling the climate change and habitability of the Earth [18,78–80]. Thus, up to now, numerous scientists have paid much attention to carbon flux calculations at oceanic subduction zones [5,15,17,37]. However, in continental collision zone settings, the evaluation of carbon flux has not received enough focus in recent years. Recently, Guo et al. (2021) [36] reported that the CO<sub>2</sub> flux of India–Asia collision-induced metamorphic decarbonation was one order of magnitude higher than that of magmatic outgassing in the Cenozoic, which implies that continent–continent collision belts can release substantial subducted carbon and act as a net carbon source [21,22,33,34,80].

To evaluate the amount of produced CO<sub>2</sub> on the orogen scale, there are still some problems to solve: (1) first of all, an estimate of the total volume of carbon-source rocks in the entire Himalayan orogen is needed [12,20,80]; (2) the duration of the CO<sub>2</sub> released is uncertain [41,43]; and (3) channelized CO<sub>2</sub> emission by fault and fracture zones [13] and/or possible carbonation reactions and CO<sub>2</sub> sequestration by carbon precipitated as graphite from a carbon-rich fluid complicates the estimate of the CO<sub>2</sub> fluxes [7–9]. Firstly, it is very sophisticated to determine the exact volume of carbon-source rocks because of the uneven distribution in different tectonic parts of the entire Himalaya. Moreover, the duration of CO<sub>2</sub>-producing reactions during prograde metamorphism is poorly constrained in the whole Himalaya ranging from 10 to 30 Ma [20,41]. As for point (3), CO<sub>2</sub> escape of the non-volcanic degassing predominantly along faults and fractures and the CO<sub>2</sub> sequestration by graphite precipitation jointly control the carbon fluxes in Himalaya, which is worthy of more in-depth analysis and discussion in future work.

The India–Asia collision-induced metamorphic decarbonation of a subducted carbonate-bearing component greatly contributes to the CO<sub>2</sub> fluxes during the Cenozoic [20,36,40–42]. The estimated flux of CO<sub>2</sub> from different kinds of literature is even an order of magnitude difference, which may result from distinct sample fields, calculation models, and the degassing rate of CO<sub>2</sub>. For example, Kerrick and Caldeira (1999) [20] reported a metamorphic CO<sub>2</sub>-producing rate of 9–24 Mt/year adopting the mass loss method in the whole GHS, whereas Becker et al. (2008) [35] and Evans et al. (2008) [34] gave the estimated CO<sub>2</sub> outgassing rate of 40 Mt/year from the Marsyandi basin of central Nepal and 8.8 Mt/year from the Narayani basin based on the carbon isotope analysis from spring waters, respectively. Rapa et al. (2017) [40] reported an estimated value of 1.4 Mt/year < CO<sub>2</sub> flux < 19.4 Mt/year using multiple component phase diagrams of calc-silicate rocks from the GHS. Groppo et al. (2020, 2022) [7,8] suggested that calcic metapelite and carbonate-poor marls should be considered as likely CO<sub>2</sub>-source rocks when modeling the global CO<sub>2</sub> degassing budget in orogenic settings. Although we did not quantify the amount of releasing CO<sub>2</sub> from the Thongmön impure marble during the prograde, peak, and retrograde metamorphism, our study potentially makes some contribution to the Himalayan CO<sub>2</sub> flux in the Eocene. It is thus significant for future work to focus more on an estimate of the total volume of the Himalaya metacarbonate rock and the duration of the CO<sub>2</sub> released on a regional scale, which helps to quantify the contribution of an orogenic belt to the global cycling. In this study, the fluid composition of the Thongmön forsterite marble is extremely H<sub>2</sub>O-rich ( $X(\text{CO}_2) < 0.04$  at 15 kbar) at the peak stage, which implies that it has experienced potential infiltration of external H<sub>2</sub>O-rich fluid. Alternatively, the fluid composition of the Thongmön forsterite marble is CO<sub>2</sub>-richer ( $0.6 < X(\text{CO}_2) < 0.8$  at 5 kbar) due to the strong overprint of regional retrogression. Thus, we suggest that the important role of orogenic settings in the global Earth's CO<sub>2</sub> tectonic outgassing should be considered.

## 7. Conclusions

This study is the first systematic work on textural relations and chemical compositions combined with metamorphic decarbonation reactions, calcite-dolomite solvus geother-

momenter, and the fluid evolution on the Thongmön impure granulite-facies marble, providing new insights into the metamorphic evolutions and metamorphic degassing processes of metacarbonate rocks in the central Himalaya. Carbonate inclusion in spinel ( $X_{Mg} = 0.153$ ) gives the highest peak temperature record ( $>780$  °C), demonstrating that the Thongmön impure marble may have gone through similar metamorphic evolution as the Thongmön metapelites. The T-X( $CO_2$ ) pseudosection at 15 kbar shows the extremely hydrous fluid ( $X(CO_2) < 0.04$ ) at peak condition of the Thongmön granulite-facies forsterite marble, which possibly results from the influx of external  $H_2O$ -rich fluid. Alternatively, after the robust retrogression overprint on a regional scale, the fluid composition of forsterite marble is  $CO_2$ -rich ( $X(CO_2) = 0.6$ – $0.8$  at 5 kbar). Thus, in either case, we suggest that the contribution of metamorphogenetic  $CO_2$  flux of impure marbles to global carbon cycling must be considered.

**Author Contributions:** Conceptualization, X.C. and L.Z.; methodology, X.C.; software, X.C.; validation, X.C. and L.Z.; formal analysis, X.C.; investigation, X.C., G.Z., Z.L. and L.Z.; resources, L.Z.; data curation, L.Z.; writing—original draft preparation, X.C.; writing—review and editing, X.C., G.Z., Z.L. and L.Z.; visualization, X.C. and L.Z.; supervision, L.Z.; project administration, L.Z.; funding acquisition, L.Z. All authors have read and agreed to the published version of the manuscript.

**Funding:** This study was supported by the National Natural Science Foundation of China (Grant no. 91755206).

**Data Availability Statement:** Not applicable.

**Acknowledgments:** We thank L.Q., W.C., L.X., L.S. and W.S. for assisting with the fieldwork. We also thank W.B. for instructive discussions. We acknowledge engineer X.L. for assisting with microprobe analyses and Antonio Langone for editorial handling. Constructive comments from Chiara Groppo and two anonymous reviewers significantly improved the manuscript.

**Conflicts of Interest:** The authors declare no conflict of interest.

## References

1. Manning, C. The chemistry of subduction-zone fluids. *Earth Planet. Sci. Lett.* **2004**, *223*, 1–16. [[CrossRef](#)]
2. Hermann, J.; Zheng, Y.F.; Rubatto, D. Deep Fluids in Subducted Continental Crust. *Elements* **2013**, *9*, 281–287. [[CrossRef](#)]
3. Bebout, G.E. Metamorphic chemical geodynamics of subduction zones. *Earth. Planet. Sci. Lett.* **2007**, *260*, 373–393. [[CrossRef](#)]
4. Liu, P.L.; Wu, Y.; Chen, Y.; Zhang, J.F.; Jin, Z.M. UHP impure marbles from the Dabie Mountains: Metamorphic evolution and carbon cycling in continental subduction zones. *Lithos* **2015**, *212–215*, 280–297. [[CrossRef](#)]
5. Alt, J.C.; Schwarzenbach, E.M.; Früh-Green, G.L.; Shanks, W.C.; Bernasconi, S.M.; Garrido, C.J.; Crispini, L.; Gaggero, L.; Padrón-Navarta, J.A.; Marchesi, C. The role of serpentinites in cycling of carbon and sulfur: Seafloor serpentinitization and subduction metamorphism. *Lithos* **2013**, *178*, 40–54. [[CrossRef](#)]
6. Omori, S.; Liou, J.G.; Zhang, R.Y.; Ogasawara, Y. Petrogenesis of impure dolomitic marble from the Dabie Mountains. *Island Arc*. **1998**, *7*, 98–114. [[CrossRef](#)]
7. Groppo, C.; Rolfo, F.; Frezzotti, M.L.  $CO_2$  outgassing during collisional orogeny is facilitated by the generation of immiscible fluids. *Commun. Earth Environ.* **2022**, *3*, 1–11.
8. Groppo, C.; Rapa, G.; Frezzotti, M.L.; Rolfo, F. The fate of calcareous pelites in collisional orogens. *J. Metamorph. Geol.* **2020**, *39*, 181–207. [[CrossRef](#)]
9. Groppo, C.; Rolfo, F.; Castelli, D.; Connolly, J.A.D. Metamorphic  $CO_2$  production from calc-silicate rocks via garnet-forming reactions in the CFAS- $H_2O$ - $CO_2$  system. *Contrib. Mineral. Petrol.* **2013**, *166*, 1655–1675. [[CrossRef](#)]
10. Castelli, D.; Rolfo, F.; Groppo, C.; Compagnoni, R. Impure marbles from the UHP Brossasco-Isasca Unit (Dora-Maira Massif, western Alps): Evidence for Alpine equilibration in the diamond stability field and evaluation of the  $X(CO_2)$  fluid evolution. *J. Metamorph. Geol.* **2007**, *25*, 587–603. [[CrossRef](#)]
11. Kato, T.M.E.; Zhai, M. Ultra-high-pressure (UHP) marble and eclogite in the Su-Lu UHP terrane, eastern China. *J. Metamorph. Geol.* **1997**, *15*, 169–182. [[CrossRef](#)]
12. Kerrick, D.M.; Caldeira, K. Paleotatmospheric consequences of  $CO_2$  released during early Cenozoic regional metamorphism in the Tethyan orogen. *Chem. Geol.* **1993**, *108*, 201–230. [[CrossRef](#)]
13. Mörrner, N.A.; Etiope, G. Carbon degassing from the lithosphere. *Glob. Planet. Change.* **2002**, *33*, 185–203. [[CrossRef](#)]
14. Racki, G. Climate changes caused by degassing of sediments during the emplacement of large igneous provinces: Comment. *Geology* **2010**, *38*, e210. [[CrossRef](#)]
15. Duncan, M.; Dasgupta, R. Rise of Earth's atmospheric oxygen controlled by efficient subduction of organic carbon. *Nature Geosci.* **2017**, *10*, 387–392. [[CrossRef](#)]

16. Menzies, C.D.; Wright, S.L.; Craw, D.; James, R.H.; Alt, J.C.; Cox, S.C.; Pitcairn, I.K.; Teagle, D.A.H. Carbon dioxide generation and drawdown during active orogenesis of siliciclastic rocks in the Southern Alps, New Zealand. *Earth Planet. Sci. Lett.* **2018**, *481*, 305–315. [[CrossRef](#)]
17. Plank, T.; Manning, C.E. Subducting carbon. *Nature* **2019**, *574*, 343–352. [[CrossRef](#)] [[PubMed](#)]
18. Stewart, E.; Ague, J.J.; Ferry, J.M.; Schiffries, C.M.; Tao, R.B.; Isson, T.T.; Planavsky, N.J. Carbonation and decarbonation reactions: Implications for planetary habitability. *Am. Min.* **2019**, *104*, 1369–1380. [[CrossRef](#)]
19. Bickle, M.J. Metamorphic decarbonation, silicate weathering and the long-term carbon cycle. *Terra Nova* **1996**, *8*, 270–276. [[CrossRef](#)]
20. Kerrick, D.M.; Caldeira, K. Was the Himalayan orogen a climatically significant coupled source and sink for atmospheric CO<sub>2</sub> during the Cenozoic? *Earth Planet. Sci. Lett.* **1999**, *173*, 195–203. [[CrossRef](#)]
21. Skelton, A. Is orogenesis a net sink or source of atmospheric CO<sub>2</sub>? *Geol. Today* **2013**, *29*, 102–107. [[CrossRef](#)]
22. Gaillardet, J.; Galy, A. Himalaya—Carbon Sink or Source? *Science* **2008**, *320*, 1727–1728. [[CrossRef](#)]
23. Ague, J.J. Fluid infiltration and transport of major, minor, and trace elements during regional metamorphism of carbonate rocks, Wepawaug Schist, Connecticut, USA. *Am. J. Sci.* **2003**, *303*, 753–816. [[CrossRef](#)]
24. Ague, J.J.; Rye, D.M. Simple models of CO<sub>2</sub> release from metacarbonates with implications for interpretation of directions and magnitudes of fluid flow in the deep crust. *J. Petrol.* **1999**, *40*, 1443–1462. [[CrossRef](#)]
25. Delpino, S.H.; Dristas, J.A. Dolomitic marbles and associated calc-silicates, Tandilia belt, Argentina: Geothermobarometry, metamorphic evolution, and P–T path. *J. S. Am. Earth. Sci.* **2008**, *25*, 501–525. [[CrossRef](#)]
26. Ferrando, S.; Groppo, C.; Frezzotti, M.L.; Castelli, D.; Proyer, A. Dissolving dolomite in a stable UHP mineral assemblage: Evidence from Cal-Dol marbles of the Dora-Maira Massif (Italian Western Alps). *Am. Min.* **2017**, *102*, 42–60. [[CrossRef](#)]
27. Trommsdorff, V. Change in T–X during metamorphism of siliceous dolomitic rocks of the Central Alps. *Schweiz. Mineral. Petrogr. Mitt.* **1972**, *52*, 567–571.
28. Castelli, D.; Rubatto, D. Stability of Al- and F-rich titanite in metacarbonate: Petrologic and isotopic constraints from a polymetamorphic eclogitic marble of the internal Sesia Zone (Western Alps). *Contrib. Mineral. Petrol.* **2002**, *142*, 627–639. [[CrossRef](#)]
29. Seaton, N.C.A.; Whitney, D.L.; Teyssier, C.; Toraman, E.; Heizler, M.T. Recrystallization of high-pressure marble (Sivrihisar, Turkey). *Tectonophysics* **2009**, *479*, 241–253. [[CrossRef](#)]
30. Satish-Kumar, M. An overview of petrology of calc-silicate granulites from the Trivandrum Block, Southern India. *J. Geosci.* **1999**, *42*, 127–159.
31. Satish-Kumar, M.; Wada, H.; Santosh, M.; Yoshida, M. Fluid-rock history of granulite facies humite-marbles from Ambasamudram, Southern India. *J. Metamorph. Geol.* **2001**, *19*, 395–410. [[CrossRef](#)]
32. Baldwin, S.L.; Fitzgerald, P.G.; Webb, L.E. Tectonics of the New Guinea Region. *Annu. Rev. Earth Planet. Sci.* **2012**, *40*, 495–520. [[CrossRef](#)]
33. Groppo, C.; Rolfo, F.; Castelli, D.; Mosca, P. Metamorphic CO<sub>2</sub> Production in Collisional Orogens: Petrological Constraints from Phase Diagram Modeling of Himalayan, Scapolite-bearing, Calc-silicate Rocks in the NKC(F)MAS(T)-HC system. *J. Petrol.* **2017**, *58*, 53–83. [[CrossRef](#)]
34. Evans, M.J.; Derry, L.A.; France-Lanord, C. Degassing of metamorphic carbon dioxide from the Nepal Himalaya, *Geochem. Geophys. Geosyst.* **2008**, *9*, Q04021. [[CrossRef](#)]
35. Becker, J.A.; Bickle, M.J.; Galy, A.; Holland, T.J.B. Himalayan metamorphic CO<sub>2</sub> fluxes: Quantitative constraints from hydrothermal springs. *Earth Planet. Sci. Lett.* **2008**, *265*, 616–629. [[CrossRef](#)]
36. Guo, Z.F.; Wilson, M.; Dingwell, D.B.; Liu, J.Q. India-Asia collision as a driver of atmospheric CO<sub>2</sub> in the Cenozoic. *Nat. Commun.* **2021**, *12*, 3891. [[CrossRef](#)] [[PubMed](#)]
37. Hoareau, G.; Bomou, B.; van Hinsbergen, D.J.J.; Carry, N.; Marquer, D.; Donnadiou, Y.; Le Hir, G.; Vrielynck, B.; Walter-Simonnet, A.-V. Did high Neo-Tethys subduction rates contribute to early Cenozoic warming? *Climate* **2015**, *11*, 1751–1767. [[CrossRef](#)]
38. Cottle, J.M.; Searle, M.P.; Horstwood, M.S.; Waters, D.J. Timing of Midcrustal Metamorphism, Melting, and Deformation in the Mount Everest Region of Southern Tibet Revealed by U(–Th)–Pb Geochronology. *J. Geol.* **2009**, *117*, 643–664. [[CrossRef](#)]
39. Li, Q.Y.; Zhang, L.F.; Fu, B.; Bader, T.; Yu, H.L. Petrology and zircon U–Pb dating of well-preserved eclogites from the Thongmön area in central Himalaya and their tectonic implications. *J. Metamorph. Geol.* **2019**, *37*, 203–226. [[CrossRef](#)]
40. Li, Q.Y.; Zhang, L.F.; Chu, X.; Zhang, G.B.; Bader, T.; Wang, Y.; Wu, C.G. Metamorphic PT path, U–Pb zircon dating and tectonic implications of High-pressure Pelitic Granulites from the Kharta region, Southern Tibet, China. *Gondwana Res.* **2021**, *104*, 23–38. [[CrossRef](#)]
41. Rapa, G.; Groppo, C.; Rolfo, F.; Petrelli, M.; Mosca, P.; Perugini, D. Titanite-bearing calc-silicate rocks constrain timing, duration and magnitude of metamorphic CO<sub>2</sub> degassing in the Himalayan belt. *Lithos* **2017**, *292–293*, 364–378. [[CrossRef](#)]
42. Rolfo, F.; Groppo, C.; Mosca, P.; Ferrando, S.; Costa, E.; Kaphle, K.P. Metamorphic CO<sub>2</sub> degassing in the active Himalayan orogen: Exploring the influence of orogenic activity on the long-term global climate changes. In *Engineering Geology for Society and Territory—Volume 1*; Lollino, M.G., Clague, A., Shan, J., Chiarle, W.M., Eds.; Springer: Berlin/Heidelberg, Germany, 2015; pp. 21–25. [[CrossRef](#)]
43. Rolfo, F.; Groppo, C.; Mosca, P. Metamorphic CO<sub>2</sub> production in calc-silicate rocks from the eastern Himalaya. *Ital. J. Geosci.* **2017**, *136*, 28–38. [[CrossRef](#)]

44. Ague, J.J. Release of CO<sub>2</sub> from carbonate rocks during regional metamorphism of lithologically heterogeneous crust. *Geology* **2000**, *28*, 1123–1126. [[CrossRef](#)]
45. Skelton, A. Flux rates for water and carbon during greenschist facies metamorphism. *Geology* **2011**, *39*, 43–46. [[CrossRef](#)]
46. Liu, G.; Einsele, G. Sedimentary history of the Tethyan basin in the Tibetan Himalayas. *Geol. Rundsch.* **1994**, *83*, 32–61. [[CrossRef](#)]
47. Liu, G.; Einsele, G. Jurassic sedimentary facies and paleogeography of the former Indian passive margin in southern Tibet. In *Himalaya and Tibet: Mountain Roots to Mountain Tops*; Macfarlane, A., Sorkhabi, R.B., Quade, J., Eds.; Geological Society of America Special Papers: Boulder, CO, USA, 1999; pp. 75–108. [[CrossRef](#)]
48. Yin, A. Cenozoic tectonic evolution of the Himalayan orogen as constrained by along-strike variation of structural geometry, exhumation history, and foreland sedimentation. *Earth Sci. Rev.* **2006**, *76*, 1–131. [[CrossRef](#)]
49. Upreti, B.N. An overview of the stratigraphy and tectonics of the Nepal Himalaya. *J. Asian Earth Sci.* **1999**, *17*, 577–606. [[CrossRef](#)]
50. Crouzet, C.; Appel, E.; Bay, R.E.; Ding, L.; Wauschkuhn, B. Kinematics of the crust around the Ama Drime massif (southern Tibet)—constraints from paleomagnetic results. *J. Asian Earth Sci.* **2012**, *58*, 119–131. [[CrossRef](#)]
51. Jessup, M.J.; Newell, D.L.; Cottle, J.M.; Berger, A.L.; Spotila, J.A. Orogen-parallel extension and exhumation enhanced by denudation in the trans-Himalayan Arun River gorge, Ama Drime Massif, Tibet-Nepal. *Geology* **2008**, *36*, 587–590. [[CrossRef](#)]
52. Burchfiel, B.C.; Chen, Z.L.; Hodges, K.V.; Liu, Y.P.; Royden, L.H.; Deng, C.R. The South Tibetan Detachment System, Himalayan orogen: Extension contemporaneous with and parallel to shortening in a collisional mountain Belt. *Geol. Soc. Am. Spec. Pap.* **1992**, *269*, 1–41. [[CrossRef](#)]
53. Kali, E.; Leloup, P.H.; Arnaud, N.; Mahéo, G.; Liu, D.; Boutonnet, E.; Van der Woerd, J.; Liu, X.; Liu-Zeng, J.; Li, H. Exhumation history of the deepest central Himalayan rocks, Ama Drime range: Key pressure-temperature-deformation-time constraints on orogenic models. *Tectonics* **2010**, *29*, TC2014. [[CrossRef](#)]
54. Borghi, A.; Castelli, D.; Lombardo, B.; Visoná, D. Thermal and baric evolution of garnet granulites from the Kharta region of S Tibet, E Himalaya. *Eur. J. Mineral.* **2003**, *15*, 401–418. [[CrossRef](#)]
55. Kohn, M.J. Himalayan metamorphism and its tectonic implications. *Annu. Rev. Earth Planet. Sci.* **2014**, *42*, 381–419. [[CrossRef](#)]
56. Lombardo, B.; Rolfo, F. Two contrasting eclogite types in the Himalayas: Implications for the Himalayan orogeny. *J. Geodyn.* **2000**, *30*, 37–60. [[CrossRef](#)]
57. Bucher, K.; Grapes, R. *Petrogenesis of Metamorphic Rocks*, 8th ed.; Springer: Berlin-Heidelberg, Germany, 2011; p. 233. [[CrossRef](#)]
58. Proyer, A.; Mposkos, E.; Baziotis, I.; Hoinkes, G. Tracing high-pressure metamorphism in marbles: Phase relations in high-grade aluminous calcite-dolomite marbles from the Greek Rhodope massif in the system CaO-MgO-Al<sub>2</sub>O<sub>3</sub>-SiO<sub>2</sub>-CO<sub>2</sub> and indications of prior aragonite. *Lithos* **2008**, *104*, 119–130. [[CrossRef](#)]
59. Warr, L.N. IMA–CNMNC approved mineral symbols. *Mineral. Mag.* **2021**, *85*, 291–320. [[CrossRef](#)]
60. Mposkos, E.; Baziotis, I.; Proyer, A.; Hoinkes, G. Dolomitic marbles from the ultrahigh-pressure metamorphic Kimi complex in Rhodope, NE Greece. *Mineral. Petrol.* **2006**, *88*, 341–362. [[CrossRef](#)]
61. Li, X.L.; Zhang, L.F.; Wei, C.J.; Slabunov, A.I.; Bader, T. Quartz and orthopyroxene exsolution lamellae in clinopyroxene and the metamorphic P–T path of Belomorian eclogites. *J. Metamorph. Geol.* **2018**, *36*, 1–22. [[CrossRef](#)]
62. Beyssac, O.; Goffé, B.; Chopin, C.; Rouzaud, J.N. Raman spectra of carbonaceous material in metasediments: A new geothermometer. *J. Metamorph. Geol.* **2003**, *20*, 859–871. [[CrossRef](#)]
63. Evans, B.W.; Trommsdorff, V. Fluorine hydroxyl titanian clinohumite in alpine recrystallized garnet peridotite: Compositional controls and petrologic significance. *Am. J. Sci.* **1983**, *283*, 355–369.
64. Ehlers, K.; Hoinkes, G. Titanian chondrodite and clinohumite in marbles from the Ötztal crystalline basement. *Mineral. Petrol.* **1987**, *36*, 13–25. [[CrossRef](#)]
65. Anovitz, L.M.; Essene, E.J. Phase Equilibria in the System CaCO<sub>3</sub>-MgCO<sub>3</sub>-FeCO<sub>3</sub>. *J. Petrol.* **1987**, *28*, 389–415. [[CrossRef](#)]
66. Hermann, J.; Troitzsch, U.; Scott, D. Experimental subsolidus phase relations in the system CaCO<sub>3</sub>-CaMg(CO<sub>3</sub>)<sub>2</sub> up to 6.5 GPa and implications for subducted marbles. *Contrib. Mineral. Petrol.* **2016**, *171*, 1–17. [[CrossRef](#)]
67. Mizuochi, H.; Satish-Kumar, M.; Motoyoshi, Y.; Michibayashi, K. Exsolution of dolomite and application of calcite-dolomite solvus geothermometry in high-grade marbles: An example from Skallevikshalsen, East Antarctica. *J. Metamorph. Geol.* **2010**, *28*, 509–526. [[CrossRef](#)]
68. Fisler, D.K.; Cygan, R.T. Cation diffusion in calcite: Determining closure temperatures and the thermal history for the Allan Hills 84001 meteorite. *Meteorit. Planet. Sci.* **1998**, *33*, 785–789. [[CrossRef](#)] [[PubMed](#)]
69. Connolly, J.A.D. Multivariable phase diagrams: An algorithm based on generalized thermodynamics. *Am. J. Sci.* **1990**, *290*, 666–718. [[CrossRef](#)]
70. Connolly, J.A.D. The geodynamic equation of state: What and how, *Geochem. Geophys. Geosyst.* **2009**, *10*, Q10014. [[CrossRef](#)]
71. Holland, T.J.B.; Powell, R. An internally consistent thermodynamic data set for phases of petrological interest. *J. Metamorph. Geol.* **1998**, *16*, 309–343. [[CrossRef](#)]
72. Tajcmanova, L.; Connolly, J.A.D.; Cesare, B. A thermodynamic model for titanium and ferric iron solution in biotite. *J. Metamorph. Geol.* **2009**, *27*, 153–165. [[CrossRef](#)]
73. Dale, J.; Holland, T.; Powell, R. Hornblende-garnet-plagioclase thermobarometry: A natural assemblage calibration of the thermodynamics of hornblende. *Contrib. Mineral. Petrol.* **2000**, *140*, 353–362. [[CrossRef](#)]
74. Proyer, A.; Rolfo, F.; Castelli, D.; Compagnoni, R. Diffusion-controlled metamorphic reaction textures in an ultrahigh-pressure impure calcite marble from Dabie Shan, China. *Eur. J. Mineral.* **2014**, *26*, 25–40. [[CrossRef](#)]

75. Bucher, K. Mechanism of mineral reactions inferred from textures of impure dolomitic marbles from East Greenland. *J. Petrol.* **1982**, *23*, 325–343. [[CrossRef](#)]
76. Perraki, M.; Faryad, S.W. First finding of microdiamond, coesite and other UHP phases in felsic granulites in the moldanubian zone: Implications for deep subduction and a revised geodynamic model for variscan orogeny in the bohemian massif. *Lithos* **2014**, *202–203*, 157–166. [[CrossRef](#)]
77. Buick, I.S.; Cartwright, I.; Williams, I.S. High-temperature Retrogression of Granulite-facies Marbles from the Reynolds Range Group, Central Australia: Phase Equilibria, Isotopic Resetting and Fluid Fluxes. *J. Petrol.* **1997**, *38*, 877–910. [[CrossRef](#)]
78. Dasgupta, R.; Hirschmann, M.M. The deep carbon cycle and melting in earth's interior. *Earth. Planet. Sci. Lett.* **2010**, *298*, 1–13. [[CrossRef](#)]
79. Selverstone, J.; Gutzler, D.S. Post-125 Ma carbon storage associated with a continent-continent collision. *Geology* **1993**, *21*, 885–888. [[CrossRef](#)]
80. Kerrick, D.M.; Caldeira, K. Metamorphic CO<sub>2</sub> degassing from orogenic belts. *Chem. Geol.* **1998**, *145*, 213–232. [[CrossRef](#)]